PHYSICAL REVIEW C **86**, 014312 (2012)

# Lifetime of the $2_1^+$ state in $^{10}$C

E. A. McCutchan,[1,2] C. J. Lister,[1] Steven C. Pieper,[1] R. B. Wiringa,[1] D. Seweryniak,[1] J. P. Greene,[1] P. F. Bertone,[1] M. P. Carpenter,[1] C. J. Chiara,[1,3] G. Gürdal,[4] C. R. Hoffman,[1] R. V. F. Janssens,[1] T. L. Khoo,[1] T. Lauritsen,[1] and S. Zhu[1]

[1]*Physics Division, Argonne National Laboratory, Argonne, Illinois 60439, USA*

[2]*NNDC, Brookhaven National Laboratory, Upton, New York 11973, USA*

[3]*Department of Chemistry and Biochemistry, University of Maryland, College Park, Maryland 20742, USA*

[4]*Nuclear Engineering Division, Argonne National Laboratory, Argonne, Illinois 60439, USA*

(Received 13 January 2012; published 9 July 2012)

The lifetime of the $J^\pi = 2_1^+$ state in $^{10}$C was measured using the Doppler shift attenuation method following the inverse kinematics $p(^{10}\mathrm{B}, n)^{10}\mathrm{C}$ reaction at 95 MeV. The $2_1^+$ state, at 3354 keV, has $\tau = 219 \pm (7)_{\mathrm{stat}} \pm (10)_{\mathrm{sys}}$ fs, corresponding to a $B(E2)\downarrow$ of 8.8(3) $e^2$ fm$^4$. This measurement, combined with that recently determined for $^{10}$Be [9.2(3) $e^2$ fm$^4$], provides a unique challenge to *ab initio* calculations, testing the structure of these states, including the isospin symmetry of the wave functions. Quantum Monte Carlo calculations using realistic two- and three-nucleon Hamiltonians that reproduce the $^{10}$Be $B(E2)$ value generally predict a larger $^{10}$C $B(E2)$ probability but with considerable sensitivity to the admixture of different spatial symmetry components in the wave functions and to the three-nucleon potential used.

DOI: 10.1103/PhysRevC.86.014312 PACS number(s): 23.20.−g, 21.10.Tg, 21.60.De, 27.20.+n

## I. INTRODUCTION

A new generation of *ab initio* calculations based on realistic nucleon-nucleon forces has deepened our understanding of how nuclei work. Comparison of their predictions to precise new experimental data [1–3] has guided improvements in the calculations, both in the computational methods used and in the underlying Hamiltonians. Electromagnetic decay rates have already proved to be surprisingly sensitive for probing three-body forces [4]. In this paper we examine mirror symmetry in nuclei, comparing $^{10}$Be to $^{10}$C, the lightest $T = 1$ mirror pair for which bound excited states exist. We have precisely measured the $B(E2; 2_1^+ \rightarrow 0_1^+)$ from the only bound state in $^{10}$C and compared it to its analog in $^{10}$Be to probe the subtleties of the symmetry. The experimental result is difficult to reproduce using our Green's function Monte Carlo (GFMC) method. A variety of calculations have been performed in order to better understand the issues.

Conceptually, the $A = 10$ mirror nuclei are interesting. $^{10}_{4}\mathrm{Be}_6$ can be thought of as two $\alpha$ particles with isospin $T = 0$, bound to a correlated pair of $s$-wave neutrons, which are usually outside the $\alpha$ clusters. Similarly $^{10}_{6}\mathrm{C}_4$ consists of two $\alpha$ particles surrounded by a loosely bound pair of protons. Naively one might expect the two protons to result in a bigger $B(E2)$ value for $^{10}$C than for $^{10}$Be. For example, a simple classical isoscalar liquid drop model [5] is driven by charge: The carbon isotope has a larger quadrupole moment ($\sim Z$) and the decay strength is expected to be larger in $^{10}$C compared to $^{10}$Be by a factor $(6/4)^2 = 2.25$. In contrast, simple shell models [6,7] always have properly constructed quantum-mechanical wave functions for states and allow the electromagnetic decay to be separated into isoscalar and isovector components. For the $A = 10$ system, the isovector contributions are predicted to be small and symmetric and act to enhance the decay in $^{10}$Be and suppress it in $^{10}$C, resulting in a $^{10}$C decay that should be $\sim$10% lower than that in $^{10}$Be. The relative $B(E2)$ values in $^{10}$C and $^{10}$Be thus represent an interesting test of nuclear modeling and of the isospin dependence of electromagnetic decays.

Within the $A = 10$ system, $^{10}$C is the more exotic partner. It has only one bound excited state, with $J^\pi = 2^+$, at 3354 keV. It becomes unbound at 4006 keV at which point it can disintegrate into $^9\mathrm{B} + p$. Its mirror partner, $^{10}$Be, has six bound states below a breakup threshold of 6812 keV where the $^9\mathrm{Be} + n$ channel opens. The first excited state of $^{10}$Be also has $J^\pi = 2^+$ and lies at 3368 keV, a sign that, in excitation energy at least, these configurations are similar, despite the difference in binding energy.

A pioneering Doppler shift attenuation method (DSAM) experiment by Fisher *et al.* [8] in 1968 was aimed at understanding these issues and testing the intermediate-coupling shell model predictions by measuring the decay rates from the first excited states in $^{10}$C and $^{10}$Be. However, the DSAM technique was new and only $\sim$20% precision could be achieved. $^{10}$C was found to be slightly more collective, but not in glaring disagreement with the shell model, given the large experimental uncertainties. We have recently remeasured the lifetime of the $2_1^+$ state in $^{10}$Be [4] and determined $B(E2; 2_1^+ \rightarrow 0_1^+) = 9.2(3)\ e^2$ fm$^4$. Comparing this with the value $B(E2; 2_1^+ \rightarrow 0_1^+) = 12.2 \pm 1.9\ e^2$ fm$^4$ measured by Fisher *et al.* for $^{10}$C still supports a larger $B(E2)$ rate in $^{10}$C. However, the carbon value has substantial experimental uncertainties, so now, with far superior experimental tools and much refined theory, we can readdress this interesting problem at a level of precision which should provide stringent tests of *ab initio* calculations.

## II. EXPERIMENT

The $2_1^+$ state in $^{10}$C was populated in the inverse kinematics $p(^{10}\mathrm{B}, n)^{10}\mathrm{C}$ reaction. Beams of $^{10}$B ions of $\sim$1 pnA and 95 MeV were produced by the ATLAS accelerator at Argonne National Laboratory. Targets consisted of thin layers of $CH_2$ on thick backings of copper and gold. $^{10}$C nuclei recoiling along

 

the beam direction were selected by the Argonne Fragment Mass Analyzer (FMA) [9] positioned 90 cm downstream of the target and subtending 1° around the beam direction. The $^{10}$C nuclei were produced at recoil velocities of $\beta = v/c \sim 13\%$ and emerged from the backing target layer with $\beta \sim 10\%$. To satisfy the FMA energy acceptance window, the recoils had to be further slowed down to $\beta \sim 8\%$. This was achieved through a series of titanium degrader foils placed at the entrance to the FMA. $^{10}$C ions with $q = 6^+$ were transported to the focal plane while most noninteracting beam particles were rejected by the FMA. The selection of $q = 6^+$ ions was very effective for suppressing scattered beam particles. The transmitted ions first passed through two Parallel Plate Avalanche Counter (PPAC) detectors before being stopped 50 cm behind the focal plane in a 30-cm-deep, two-electrode ionization-chamber operated at 50 torr. $\gamma$ rays were detected with the Gammasphere array [10] consisting of 100 Compton-suppressed High Purity Germanium (HPGe) detectors in 16 azimuthally symmetric rings from $\theta = 34°$ to 163° relative to the beam direction.

Figure 1(a) shows a typical energy loss ($\Delta E$) versus total energy ($E_{\rm tot}$) spectrum obtained from the ionization chamber. The locus with the largest $\Delta E$ (solid red circled region) corresponds to direct population of the $2_1^+$ state in $^{10}$C. The large spread in total energy for these recoils stems from energy scattering and straggling in the backing and degrader foils. The wide strip of counts below the $^{10}$C recoils is identified with $^{10}$B scattered beam. The pressure in the ionization chamber was not sufficient to fully stop the highest energy $^{10}$C recoils, resulting in a wraparound feature (punch through) in the $\Delta E$ versus $E_{\rm tot}$ plot. Direct population of the ground state of $^{10}$C is also observed, although owing to the punch through, it appears in the same $\Delta E$ versus $E_{\rm tot}$ area as the $^{10}$B scattered beam. The $\gamma$-ray spectrum obtained by gating on the excited $^{10}$C recoils is given in Fig. 1(b), showing only the 3354-keV, $2_1^+ \rightarrow 0_1^+$ transition in $^{10}$C.

The current setup offers several advantages over the prior DSAM measurement performed with a regular-kinematics reaction. To compare the present technique with a normal kinematics DSAM measurement, the original Fisher *et al.* experiment [8] was also repeated with Gammasphere. This regular-kinematics experiment was performed with a 9.5-MeV proton beam incident on a $^{10}$B target followed by a gold backing. $\gamma$ rays were detected with the Gammasphere array. A comparison of the spectra obtained from the regular- and inverse-kinematics reactions is given in Fig. 2 for the same angle group ($\theta = 130°$) in Gammasphere. The regular kinematics spectrum [Fig. 2(a)] is very complicated, with considerable background from reactions of the high-energy protons on the $^{10}$B target, the gold backing, and scattering in the target chamber. In contrast, requiring detection of a recoiling $^{10}$C residue by the FMA almost entirely suppresses the background [Fig. 2(b)], providing a spectrum where only the $2_1^+ \rightarrow 0_1^+$ transition in $^{10}$C is observed. Selection of the $^{10}$C recoils with the FMA also provides a well-defined angle between the recoil velocity vector and the direction (and subsequent detection) of the $\gamma$ rays. Recoil detection comes at the cost of poorer statistics; however, with almost no background the peak centroids can be reliably determined to

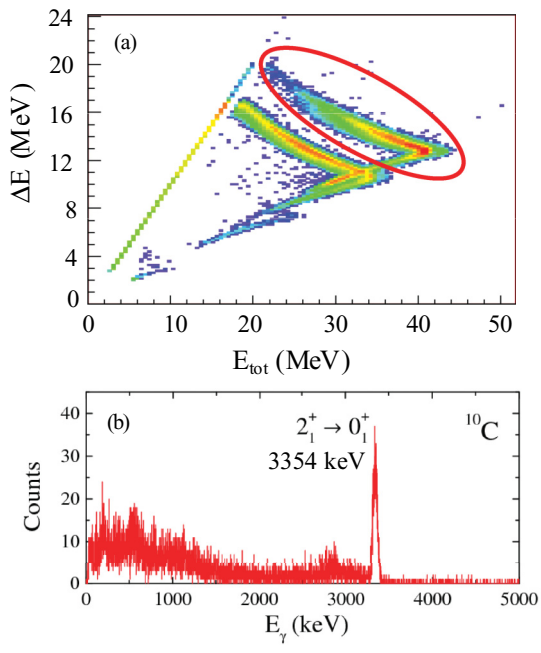


FIG. 1. (Color online) (a) Energy loss versus total energy plot of data from the ionization chamber behind the focal plane of the FMA. The solid red circled region is direct population of the $2_1^+$ state in $^{10}$C. Data were obtained with a 116 $\mu$g/cm$^2$ $CH_2$ target on a 23.8 mg/cm$^2$ copper backing. (b) $\gamma$-ray spectrum obtained by gating on the excited $^{10}$C recoils.

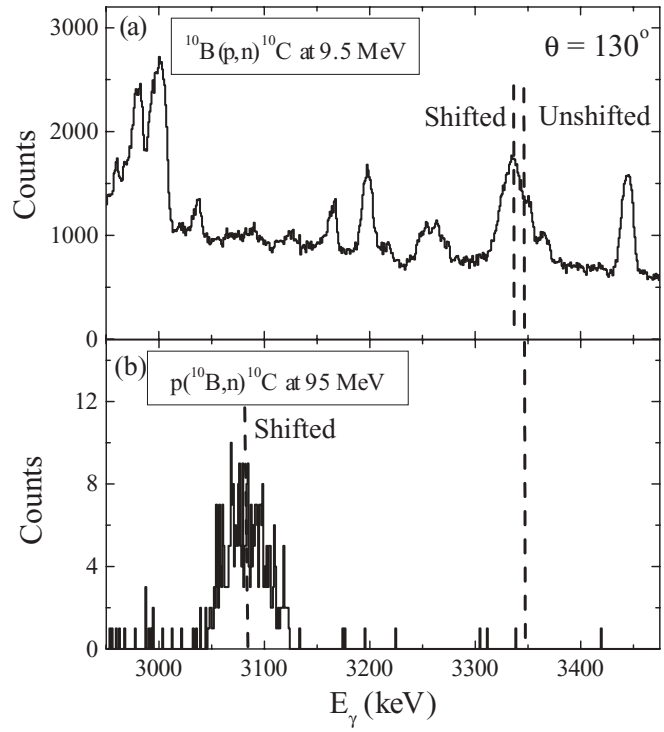


FIG. 2. Comparison of $\gamma$-ray spectra for $^{10}$C decays from DSAM in (a) regular and (b) inverse kinematics. Both spectra correspond to the $\theta = 130°$ angle group in Gammasphere. Reaction details are included in the figure.

1–2 keV. With the regular-kinematics reaction, the recoiling $^{10}$C ions have a kinetic energy of a few MeV, an energy regime where stopping powers are poorly determined and the $\gamma$-ray energy shifts are only a few keV. In the inverse-kinematics reaction, $^{10}$C nuclei were produced at a very high recoil energy ($E \sim 80$ MeV). This allows the measurement to be performed in a velocity regime where the stopping is 99.99% electronic and most precisely known. The high recoil velocity also produces large Doppler shifts. With the set of Gammasphere angles, the range of forward-shifted to backward-shifted peaks spanned more than 800 keV.

In a DSAM measurement the lifetime is derived from the difference between production and emission velocities. For the inverse-kinematics reaction, the distribution of recoil products is very forward peaked and there are two solutions for residues moving along the initial beam direction, depending on the direction of the emitted neutron. For this particular experiment, recoils emitted at 0° relative to the beam direction can have recoil velocities of 75 or 82 MeV. The FMA was always set to transmit the higher-energy recoil group. The initial $\beta$ value at production is first measured using a self-supporting $CH_2$ target and correcting for the small energy loss in the target. Degrader foils of the same thickness as the backed-target experiments were used to replicate the DSAM measurements and ensure that the FMA entrance conditions were the same for both the self-supporting and the backed targets.

To determine the average velocity of the recoils at the time of $\gamma$-ray emission, the centroid of the 3354-keV, $2_1^+ \rightarrow 0_1^+$ transition was determined for each of the 16 Gammasphere angle rings. In Fig. 3(a), the measured centroid is plotted as a function of $\cos(\theta)$ for a 105 $\mu$g/cm$^2$ $CH_2$ target on a 23 mg/cm$^2$ copper backing. A fit to these data yields an average $\beta$ at the time of $\gamma$-ray emission of $\beta = 0.124\,22(24)$. For reference, a lifetime of $\tau \sim 0$ would give $\beta \sim 0.131$ (the production velocity) while an infinitely long lifetime would yield $\beta \sim 0.099$ (velocity after emerging from the backing layer). The measured centroids are compared to the relativistic Doppler shift formula using the best fit $\beta$ in Fig. 3(a). Figure 3(b) illustrates the quality of the fit more clearly, by dividing the measured centroids by the function $\sqrt{1-\beta^2}/[1-\beta\cos(\theta)]$. Included are lines for $\beta$ values for the best fit $\beta$ ($\beta = 0.124\,22$, corresponding to $\tau = 224$ fs), production ($\beta = 0.131$, corresponding to $\tau = 0$), and that which would correspond to the previous lifetime value ($\beta = 0.1265$ for $\tau = 154$ fs).

To determine the lifetime of the level of interest from the measured mean $\beta$ value, the thicknesses of the target and backing layers must be known, as this defines the relevant transit time scale. The backing foils were prepared by rolling gold and copper foils to the appropriate thickness. Targets were then prepared by dipping the backing foils into solutions of xylene and $C_2H_2$ and subsequently evaporating the xylene. The thin layer of $CH_2$ on a very thick backing of gold or copper made a precise measurement of the $CH_2$ thickness by a traditional $\alpha$-gauging method impossible. The $CH_2$ thickness was determined by comparing the yield (number of $^{10}$C recoils detected in the ionization chamber, per beam intensity, per time) of a backed target relative to a commercially made self-supporting $CH_2$ target of known thickness. A series of degrader

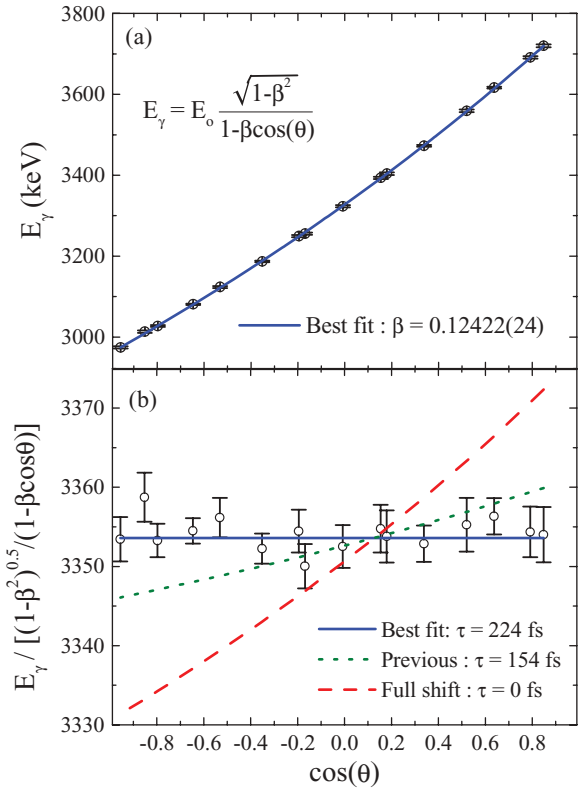


FIG. 3. (Color online) (a) Measured centroids of the 3354-keV transition for each Gammasphere angle group. The solid curve shows the result of the relativistic Doppler shift formula taking the best-fit value of $\beta$. (b) Similar to (a) but normalized to $\sqrt{1-\beta^2}/[1-\beta\cos(\theta)]$. Lines include the best fit value of $\beta$ (solid line), maximum $\beta$ value allowed by the reaction kinematics (dashed line), and the $\beta$ value corresponding to the previous lifetime measurement (dotted line).

foils, identical to the target backing, were placed behind the self-supporting $CH_2$ target to achieve the same energy recoils into the FMA as with the backed targets. The thickness of the $CH_2$ layer on the backed targets was measured before and after the DSAM measurement via a relative yield measurement, as described above. An approximately 20% reduction in yield was observed. For the DSAM analysis, the average of the thickness before and after the measurement was used and the full range of thickness taken as the uncertainty. As the target layers are thin and do not provide much stopping and the ions move very quickly through them, the target thickness does not contribute greatly to the systematic uncertainty. The characterization of carbon and boron ions slowing in $CH_2$, copper, and gold was taken from the SRIM [11] and MSTAR [12] packages. The two models differ in stopping powers on the order of 3% in the relevant velocity regime. These differences were incorporated into the systematic uncertainty.

The lifetime of the 3354-keV level was measured in five separate experiments. The target characteristics and the extracted lifetimes are summarized in Table I. The weighted mean value is $\tau = 219 \pm (7)_{\text{stat}} \pm (10)_{\text{syst}}$ fs, which implies $B(E2; 2_1^+ \rightarrow 0_1^+) = 8.8(3)\ e^2\ \text{fm}^4$. This lifetime is substantially longer than the previous value obtained by Fisher *et al.*

TABLE I. Mean lifetimes from different target and backing combinations determined for the 3354-keV level in $^{10}$C. The $CH_2$ thicknesses are the average of the measured values at the beginning and end of each DSAM measurement.

| Target ($CH_2$) ($\mu$g/cm$^2$) | Backing (mg/cm$^2$) | $\tau$ (fs) | $\Delta\tau_{stat}$ (fs) |
|---|---|---|---|
| 105 | 23.0 Cu | 224 | ±8 |
| 150 | 31.0 Au | 215 | ±10 |
| 170 | 23.8 Cu | 219 | ±13 |
| 80 | 24.0 Au | 198 | ±18 |
| 300 | 14.9 Au | 216 | ±23 |

[8]. Figure 4 gives a comparison of the current measurements (solid symbols) and those of Ref. [8] (open symbols). Clearly, the data are now much better constrained for investigating the symmetry of the wave functions, but theoretical guidance is needed to infer the meaning of the result.

## III. THEORY

Empirically, assuming charge symmetry for the wave functions, the transition strengths can be written as

$$B(E2) = [M(E2)]^2/5 = [A + BT_z]^2, \quad (1)$$

where $M(E2)$ is the reduced matrix element and we use the convention that $T_z = +\frac{1}{2}$ for the neutron. The new $^{10}$Be and $^{10}$C data can be used to infer that the isoscalar term is dominant, $A = 3.00(1)\ e\ \mathrm{fm}^2$, while the isovector term is much smaller, $B = 0.03(3)\ e\ \mathrm{fm}^2$, a 1% effect. In conventional shell-model calculations, isospin enhancements or effective charges, $\epsilon(T)$ are introduced to account for effects such as core polarization: $A = A'\epsilon(0)$ and $B = B'\epsilon(1)$, where $A'$ and $B'$ are constants derived for a particular wave function. Very early shell model calculations of Cohen and Kurath [6,13] for the mass 10 system gave predictions for $B(E2)$ strengths in the form of Eq. (1). These are included in Fig. 4 (solid black line).

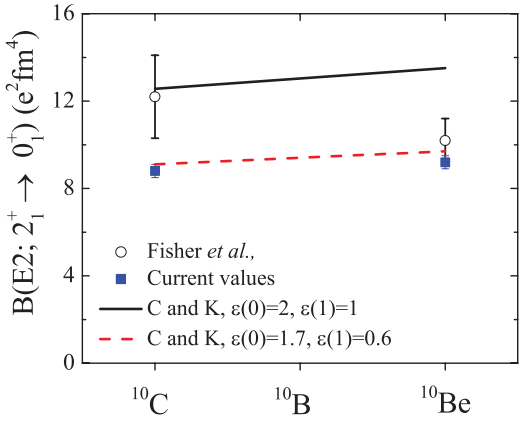


FIG. 4. (Color online) $B(E2; 2_1^+ \rightarrow 0_1^+)$ transition strengths (in $e^2$ fm$^4$) for $^{10}$C and $^{10}$Be. Open symbols are the results of Fisher *et al.* [8], while solid symbols are the current work and the recent measurement of Ref. [4]. Solid and dashed lines are shell model calculations using different values for effective charges.

These $p$-shell, mirror-symmetric wave functions provide the correct slope for describing the transition strengths between $^{10}$C and $^{10}$Be, however, overestimate the overall magnitude (Fig. 4) owing to the use of very simple isoscalar and isovector enhancements, $\epsilon(0) = 2$ and $\epsilon(1) = 1$. Using isoscalar and isovector enhancements now broadly accepted for $p$-shell calculations [14,15], $\epsilon(0) = 1.7$ and $\epsilon(1) = 0.6$, one obtains $^{10}$Be $B(E2; 2_1^+ \rightarrow 0_1^+) = 9.7e^2$ fm$^4$ and $^{10}$C $B(E2; 2_1^+ \rightarrow 0_1^+) = 9.1\ e^2$ fm$^4$. These calculations are included in Fig. 4 (dashed red line).

Clearly, the simple shell model does an excellent job of reproducing both the trend in $B(E2)$ values between $^{10}$C and $^{10}$Be, as well as the absolute magnitude. While this is a testament to the predictive power of the shell model, it is perhaps not surprising as the Hamiltonian has been tuned to reproduce the energies of $p$-shell nuclei and the effective charges are fitted to $B(E2)$ data. Furthermore, while the results tend to suggest mirror symmetry in the wave functions of $^{10}$C and $^{10}$Be, a chance cancellation of subtle effects cannot be ruled out. Mirror symmetry in the shell model calculations implies a dominant isoscalar term along with nearly zero isovector contributions to the $B(E2)$ strengths. With the present set of data and shell-model calculations, one cannot rule out the possibility that the isoscalar term actually differs in $^{10}$C and $^{10}$Be, but that the differences are offset by varying contributions to the isovector component. To investigate these different scenarios in more detail, we turn to more sophisticated *ab initio* models based on "bare" forces constrained by *NN* scattering data and the binding energies of light nuclei.

The variational Monte Carlo (VMC) and GFMC methods have been very useful in improving our understanding of light nuclei [16,17] and successful in reproducing the electric quadrupole collectivity in $^{10}$Be, without resorting to the use of any effective charges. Using realistic two- and three-body potentials (including explicit charge-symmetry-breaking terms), this is a good approach for exploring $^{10}$C and the symmetry of the $A = 10$ wave functions.

The details on the GFMC method of calculating transition strengths are given in Ref. [18]. Here, we outline some aspects relevant to the current discussion. The VMC calculations use trial wave functions containing noncentral two- and three-body correlation operators acting on an antisymmetrized one-body wave function, $\Phi(JMTT_z)$, which determines the quantum numbers of the state being computed. The $\Phi(JMTT_z)$ wave function is expanded in $LS$-basis functions [17]:

$$\Phi(JMTT_z) = \sum_{LS[n]} \beta(^{2S+1}L[n], JTT_z)\Phi(^{2S+1}L[n], JMTT_z), \quad (2)$$

where the amplitudes $\beta(^{2S+1}L[n], JTT_z)$ are found from a diagonalization of the Hamiltonian. For $^{10}$Be, we construct states from the three highest spatial symmetries as denoted by the Young diagram $[n]$ (see Ref. [19]). This gives three basis functions for the $0^+$ ground state: $^1$S[442], $^3$P[4411], and $^3$P[433], while the $2^+$ states have six basis functions: $^1$D[442]$_-$, $^1$D[442]$_+$, $^3$P[4411], $^3$P[433], $^3$F[4411], and $^3$F[433]. Note that there are two linearly independent

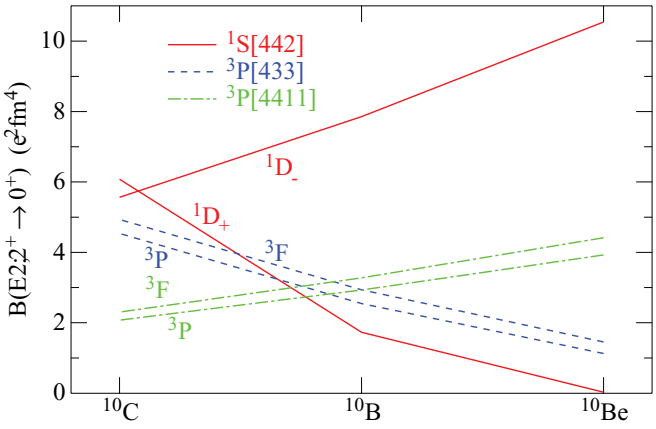


FIG. 5. (Color online) $B(E2)$ transition strengths (in $e^2$ fm$^4$) for VMC basis state pairs. Only transitions that conserve spatial symmetry are shown. The legend gives the designation of the $0^+$ states while the curves are labeled with the $^{2S+1}L$ of the $2^+$ states. The Monte Carlo statistical errors associated with the calculation are on the order of 10%.

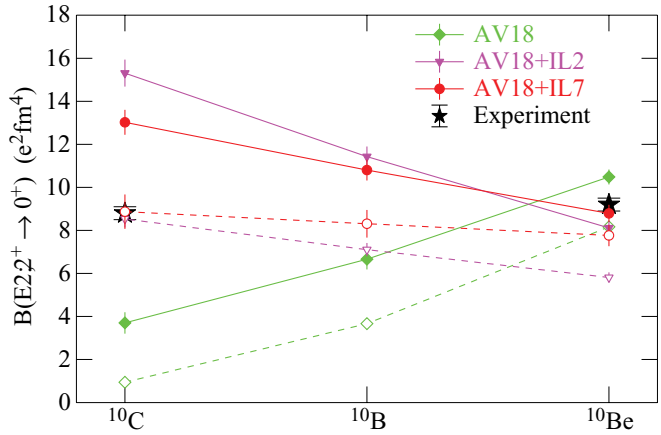


FIG. 6. (Color online) VMC and GFMC calculations of $B(E2)$ strengths for the $2_1^+$ ($Q < 0$) state assuming isospin symmetric wave functions. The wave functions were computed for $^{10}$Be using the indicated Hamiltonians. VMC results are shown as open symbols and dashed lines; GFMC results are solid symbols and solid lines.

$^1$D[442] basis states; the distinction between them is arbitrary and we choose to express them as eigenfunctions of the quadrupole operator, with the subscript indicating the sign of the quadrupole moment. The VMC $E2$ matrix element is

$$M(E2) = \sum_{L'S'[n'],LS[n]} \beta(^{2S'+1}L'[n'], J=0, T=1, T_z) \times \beta(^{2S+1}L[n], J=2, T=1, T_z) \times \langle \mathcal{C}\Phi(^{2S'+1}L'[n'], J=0, T=1, T_z) \times ||E2||\mathcal{C}\Phi(^{2S+1}L[n], J=2, T=1, T_z)\rangle, \quad (3)$$

where $\mathcal{C}$ denotes the two- and three-body correlations and there are $3 \times 6$ contributions to the sum. The isoscalar $E2$ operator does not change spatial symmetry, so the only big contributions are those from $^1$D[442]$_-$ or $^1$D[442]$_+$ to $^1$S[442], $^3$P[4411] or $^3$F[4411] to $^3$P[4411], and $^3$P[433] or $^3$F[433] to $^3$P[433] (the $\mathcal{C}$ do not conserve the spatial symmetry so there are small nonzero matrix elements for the other possibilities). These individual contributions, calculated with wave functions for the AV18 two-nucleon and Illinois-7 three-nucleon potentials (AV18 + IL7) [20,21], are shown in Fig. 5 for isospin-symmetric basis states; that is, the parameters in $\Phi(^{2S+1}L[n], J=2, M, T=1, T_z)$ are independent of $T_z$. The diagonalization of the two $^1$D[442] states into the quadrupole basis was done for $^{10}$Be and not changed for $^{10}$B and $^{10}$C.

As can be seen, these isospin-symmetric calculations can give very different $T_z$ behaviors, depending on the pair of $^{2S+1}L[n]$ states being used. In particular, while $^{10}$Be is dominated by the transition with the $^1$D[442]$_-$ component, $^{10}$C can have significant contributions from all the spatial symmetries. Calculations with basis states containing different variational parameters give very similar results to those in the figure; we believe that the trends shown result from the different $^{2S+1}L[n]$ values of the pairs and thus also would be obtained with other realistic Hamiltonians and even for the corresponding harmonic-oscillator shell model states. This means that the nearly $T_z$-independent $B(E2)$ strengths obtained in the shell model calculation require a specific combination of states.

Figure 6 shows VMC and GFMC calculations of $B(E2)$ values for the $2_1^+$ ($Q < 0$) state assuming isospin symmetric wave functions. The wave functions were computed for $^{10}$Be using the AV18 interaction alone or with the IL2 or IL7 three-body potentials. As shown in Ref. [4], the $2_1^+$ state of $^{10}$Be has a negative quadrupole moment and a strong $E2$ decay to the ground state for all the Hamiltonians. (For AV18 alone, the energies of the two $2^+$ states are nearly degenerate, so we choose to identify the $Q < 0$ state as the $2_1^+$ state.) The reduced matrix elements for $^{10}$C were obtained by interchanging protons and neutrons in the $^{10}$Be wave functions and the $^{10}$B reduced matrix elements are the average of the $^{10}$Be and $^{10}$C; that is, the wave functions are isospin symmetric with those of $^{10}$Be. There is considerable variation in the $T_z$ behavior of the $B(E2)$ strengths for the different Hamiltonians in the VMC calculations. This is presumably attributable to the different $\beta(^{2S+1}L[n], J=2, T=1, T_z=+1)$ amplitudes from the separate diagonalizations. The GFMC generally preserves, or even enhances, these different trends, which suggests a strong sensitivity of the isovector $B(E2)$ to the three-body force.

Isospin symmetry of the wave functions is certainly only an approximation. Owing primarily to the increasing Coulomb potential energy going from $^{10}$Be to $^{10}$C, the $^{10}$C states under consideration are less bound (0.5 MeV vs 3.5 MeV for the $2_1^+$ state) and, hence, should be more diffuse. This can be studied by performing separate calculations for each nucleus. We have done such calculations for the AV18 + IL7 Hamiltonian. The one-body parts of the VMC wave functions are solutions of Woods-Saxon wells plus an average Coulomb potential [17]; the strength of the Coulomb term is proportional to the number of $p$-shell protons. Separate diagonalizations were made for each nucleus, so the $\beta$ are also different. The GFMC propagations are still made in a good isospin basis, but the isoscalar Coulomb potential used reflects the total charge of

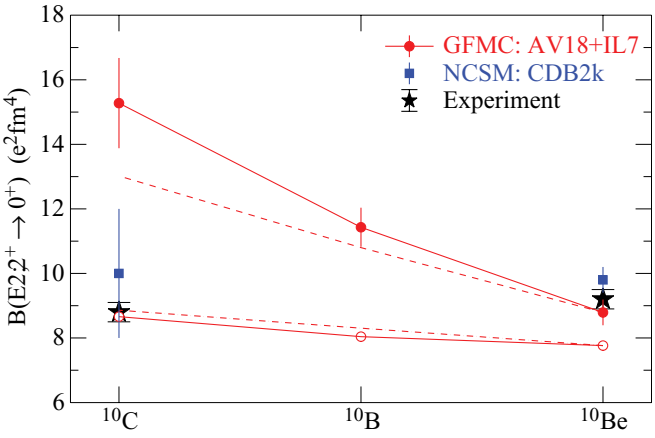


FIG. 7. (Color online) VMC and GFMC calculations of $B(E2)$ for the lowest ($Q < 0$) $2^+$ state with the AV18 + IL7 Hamiltonian. The wave functions were computed separately for each nucleus using different VMC correlations and independent GFMC propagation. VMC results are shown as open symbols; GFMC results are solid symbols. The dashed lines show the corresponding isospin symmetric results from Fig. 6.

the nucleus [18]. The results of these calculations are compared with the isospin-symmetric AV18 + IL7 calculations in Fig. 7. The independent calculations for $^{10}$C and $^{10}$B are not very different from the isospin-symmetric extrapolations from the $^{10}$Be results. Unfortunately, the already too large value for the $^{10}$C $B(E2)$ is further increased.

In light of the apparent failure of these GFMC calculations to reproduce the $B(E2; 2_1^+ \rightarrow 0_1^+)$ transition strength in $^{10}$C, it is important to consider possible shortcomings of the calculation which could cause the discrepancy. One possibility is that, with the weaker binding of the $2_1^+$ state in $^{10}$C compared to $^{10}$Be, contributions from beyond the $p$ shell might become important. In fact, the VMC trial functions already have a fair admixture of $sd$-shell and higher components owing to two-body tensor correlations in the $\mathcal{C}$ of Eq. (3) (see Ref. [16]), and these are further enhanced in the GFMC propagation. However, to further test this possibility, we constructed alternative clusterized VMC trial functions with explicit $sd$-shell components. These wave functions combine a $^8$Be($0^+$ or $2^+$) core with two final nucleons in $p$- or $sd$-shell orbitals (with appropriate Coulomb terms), all $LS$-coupled to give the appropriate total $J^\pi$. The $0^+$ ($2^+$) states have four (seven) $p$-shell and eight (seven) $sd$-shell components; separate diagonalizations for the corresponding $\beta$'s are made for each $T_z$. For a Hamiltonian containing AV18 and the Urbana IX (UIX) three-body potential [22], the $sd$-shell $\beta$'s contribute only 2.5% of the total wave function in the $^{10}$Be $0_1^+$ state, but 21% in the $0_2^+$ state; these numbers increase to 3.4% and 28.9%, respectively, in $^{10}$C. The $2_1^+$ and $2_2^+$ states both have 4% or less $sd$-shell contributions, with only slightly greater amounts in $^{10}$C than in $^{10}$Be. (Interestingly, 96% of the $2_1^+$ state has a $^8$Be($2^+$) core in this construction, clearly indicating it is the $J = 2$ member of the $K = 0$ rotational band.) Consequently, inclusion of the $sd$-shell components has only a very minor effect on the $B(E2)$ values; in $^{10}$Be using $p$-shell only components gives $B(E2) = 8.6\ e^2\ \text{fm}^4$, while adding $sd$-shell components raises it to $9.2\ e^2\ \text{fm}^4$. The corresponding $B(E2)$ values in $^{10}$C are 9.6 and 11.6 $e^2$ fm$^4$, respectively, showing the same moderate change with $T_z$ as the AV18 + IL2 and AV18 + IL7 Hamiltonians.

A more likely possibility is simply that the Hamiltonians tested are not adequate for these transitions. The first priority in theoretically modeling the nuclear Hamiltonian has been obtaining good energies for the states in question, both absolute binding energy of the nucleus and excitation energies of the higher states. These energies are shown in Table II for the various Hamiltonians used in the present GFMC calculations, along with charge radii, quadrupole moments, and the $B(E2)$ values. The AV18 + IL7 Hamiltonian gives a particularly good overall reproduction of both absolute binding and excitation energies. The charge radius for $^{10}$Be is also in excellent agreement with a recent measurement [23]. Table II and Fig. 6 indicate that while the various models tested give rather similar results for the $B(E2)$ strengths in $^{10}$Be, they give a much more widely varying range of results for $^{10}$C. The quadrupole moments also have far more variation in $^{10}$C.

The no-core shell model (NCSM) [24–26] is another *ab initio* method that has been used to compute transitions in $A = 10$ nuclei. So far, these calculations have been made with only two-nucleon potentials: Results for the CD-Bonn 2000 (CDB2k) potential [27] are given in Table II. Not surprisingly, without a three-body force the ground states are significantly underbound, but the excitation energies are reasonable. NCSM calculations are generally performed in a harmonic oscillator basis with a maximum number of excited quanta allowed, so that radial wave functions tend to fall off too rapidly at large distances. This is the probable reason for the charge radius for $^{10}$Be being too small (especially in light of the underbinding). Consequently, operators with an $r^2$ dependence such as $B(E2)$ may converge more slowly than the energy calculations. Nevertheless, the NCSM results for $B(E2)$ strengths are in excellent agreement for both the transitions in $^{10}$Be. The $^{10}$C is also very good, although there is a large error bar owing to a difficulty in separating the two $2^+$ states [25].

A number of other *ab initio* many-body methods are being developed, some of which can calculate transitions in the $A = 10$ and neighboring nuclei. The no-core Monte Carlo shell model is currently [28] being applied to both $^{10}$C and $^{10}$Be. The fermion molecular dynamics approach [29] has been used to study energies and densities in a variety of light $p$- and $sd$-shell nuclei using realistic interactions such as AV18. Results for $B(E2)$ values in beryllium isotopes have been reported in workshops, but have not yet been published [30]. A similar many-body method which emphasizes the cluster structure of light nuclei is the antisymmetric molecular dynamics [31,32] approach, but it has been used only with much simpler interactions that are not directly related to $NN$ scattering data. Coupled-cluster methods [33] are being applied to an increasing number of light- and medium-mass nuclei, but have not been used for $A = 10$ nuclei. Lattice methods have been used [34] to calculate the ground states of simple light systems, such as $N = Z$ and $\alpha$-cluster nuclei, and recently have been extended to calculate [35] the properties of excited states in $^{12}$C.

TABLE II. GFMC calculations of the $A = 10, T = 1$, ground-state energies $E_{gs}$ and excitation energies $E_x$ in MeV for several Hamiltonians used in this work, plus NCSM results for the CD-Bonn 2000 potential and experimental values. ($^{10}$B excitations are shown relative to the $0^+; 1$ isobaric analog.) Also shown are ground-state charge radii in fm, quadrupole moments for the excited states in $e\,\mathrm{fm}^2$, and the $B(E2)$ transition strengths in $e^2\,\mathrm{fm}^4$. Asterisks denote GFMC results obtained with isospin-symmetric wave functions generated from $^{10}$Be (see text). The numbers in parentheses for the GFMC calculations are Monte Carlo statistical errors; those for the NCSM results are the errors reported in Refs. [24–26].

| $^AZ$ | Observable | NCSM | GFMC | | | Expt. |
|---|---|---|---|---|---|---|
| | | CDB2k | AV18 | AV18 + IL2 | AV18 + IL7 | |
| $^{10}$Be | $\lvert E_{gs}(0^+)\rvert$ | 56.5(5) | 50.1(1) | 66.4(4) | 64.1(3) | 64.98 |
| | $E_x(2_1^+)$ | 3.6(1) | 2.9(1) | 5.0(4) | 3.4(3) | 3.37 |
| | $E_x(2_2^+)$ | 4.8(1) | 3.0(1) | 5.8(4) | 5.3(3) | 5.96 |
| | $r_c$ | 2.25(5) | 2.47(1) | 2.33(1) | 2.33(1) | 2.36(2) |
| | $Q(2_1^+)$ | −5.9(5) | −4.1(1) | −4.9(1) | −6.7(1) | |
| | $Q(2_2^+)$ | 5.3(5) | 5.8(1) | 0.2(1) | 4.5(1) | |
| | $B(E2; 2_1^+ \to 0^+)$ | 9.8(4) | 10.5(4) | 8.1(3) | 8.8(4) | 9.2(3) |
| | $B(E2; 2_2^+ \to 0^+)$ | 0.2(2) | 3.4(2) | 3.3(2) | 1.8(1) | 0.11(2) |
| $^{10}$B | $\lvert E(0^+; 1)\rvert$ | 55.3(5) | 48.3(3)* | 64.6(4)* | 62.6(2) | 63.01 |
| | $E_x(2_1^+; 1)$ | | 2.9(4)* | 5.0(5)* | 3.6(3) | 3.42 |
| | $E_x(2_2^+; 1)$ | | 3.0(4)* | 5.8(5)* | 5.2(5) | |
| | $Q(2_1^+; 1)$ | | −5.8(1)* | −3.5(1)* | −2.7(1) | |
| | $Q(2_2^+; 1)$ | | 7.9(1)* | −2.0(1)* | | |
| | $B(E2; 2_1^+; 1 \to 0^+; 1)$ | | 6.7(5)* | 11.4(5)* | 11.4(6) | |
| | $B(E2; 2_2^+; 1 \to 0^+; 1)$ | | 8.9(4)* | 1.0(1)* | | |
| $^{10}$C | $\lvert E_{gs}(0^+)\rvert$ | 51.9(5) | 45.8(3)* | 61.7(4)* | 60.0(2) | 60.32 |
| | $E_x(2_1^+)$ | 3.6(1) | 2.7(3)* | 4.7(4)* | 3.2(3) | 3.35 |
| | $E_x(2_2^+)$ | 4.3 | 2.8(3)* | 5.4(4)* | 5.1(5) | |
| | $r_c$ | | 2.77(1)* | 2.55(1)* | 2.65(1) | |
| | $Q(2_1^+)$ | −1.1(12) | −7.5(2)* | −2.1(2)* | −2.7(2) | |
| | $Q(2_2^+)$ | | 10.0(2)* | −4.2(2)* | −0.9(3) | |
| | $B(E2; 2_1^+ \to 0^+)$ | 10(2) | 3.7(5)* | 15.3(6)* | 15.3(1.4) | 8.8(3) |
| | $B(E2; 2_2^+ \to 0^+)$ | | 17.0(8)* | 0.0(1)* | 0.2(1) | |

## IV. CONCLUSIONS

We have performed a precise measurement of the lifetime of the first excited state in $^{10}$C. We have separated, investigated, and reduced many systematic errors in the Doppler shift attenuation method to obtain reliable results with less than 5% error. From data on five different targets with varying thickness of gold and copper backings, we arrive at a lifetime of $\tau = 219 \pm (7)_{\mathrm{stat}} \pm (10)_{\mathrm{sys}}$ fs for the $2_1^+$ state at 3354 keV.

From this result, we find that the electric quadrupole matrix element in $^{10}$C is only 2% different from the corresponding transition in $^{10}$Be. This finding is consistent with traditional $p$-shell shell model calculations, especially when modern effective charges are employed. However, our result has proved exceptionally difficult to reproduce using GFMC *ab initio* calculations. We have investigated many aspects of the calculation. In particular, we have done calculations with explicit isospin breaking and find these effects are small: The proton distribution in $^{10}$C is calculated to be very similar to the neutron distribution in $^{10}$Be. We have investigated the contributions of $sd$-shell occupancy in these wave functions, and again find the effects small, similar in $^{10}$C and $^{10}$Be, and insufficient to explain the discrepancy between calculation and experiment. It appears that the near-equal matrix elements arise from a specific interference of single-particle contributions and do not have a single, simple underlying cause.

The GFMC with modern three-body forces has proved very successful in reproducing the "static" properties of light nuclei, such as binding energies of states and rms radii. Indeed, these properties are what have been used to model and constrain three-body forces. Dynamic properties, such as transition rates for $\gamma$ and $\beta$ decay, are the current challenge. By investigating the individual contributions to the $B(E2)$ transition strengths, we find that while the [442] symmetry components are the dominant components of the low-lying states, the precise admixture of the lower symmetries is quite sensitive to the three-body force. Obtaining the correct mix of these components in the ground and excited states is crucial to reproducing the proper variation of the $B(E2)$ with $T_z$. It appears that our energetically best force, AV18 + IL7, does not produce the correct mixing; some modification is needed which would preserve the energy characteristics, but produce a better combination of spatial symmetry components. At the onset of this research it was not clear that electromagnetic decay rates would be very sensitive to the form of the three-body forces used. Now it emerges that some of these rates, carefully measured, may be critical for constraining the next generation of three-body forces.

## ACKNOWLEDGMENTS

Understanding our measurement for $^{10}$C has been challenging and we have had lengthy discussions with many people to try to understand its significance. We thank John Millener for discussions about the traditional $p$-shell model and Petr Navrátil for NCSM predictions. Calculations were performed on the parallel computers of the Laboratory Computing Resource Center and of the Mathematics and Computer Science Division, Argonne National Laboratory. This work was supported by the DOE Office of Nuclear Physics under Contracts No. DE-AC02-06CH11357 and No. DE-AC02-98CH10946, Grant No. DE-FG02-94-ER40834, and SciDAC Grant No. DE-FC02-07ER41457.



[1] A. H. Wuosmaa *et al.*, Phys. Rev. Lett. **94**, 082502 (2005).
[2] P. Mueller *et al.*, Phys. Rev. Lett. **99**, 252501 (2007).
[3] G. F. Grinyer *et al.*, Phys. Rev. Lett. **106**, 162502 (2011).
[4] E. A. McCutchan *et al.*, Phys. Rev. Lett. **103**, 192501 (2009).
[5] A. Bohr and B. R. Mottleson, *Nuclear Structure* (World Scientific, Singapore, 1998).
[6] S. Cohen and D. Kurath, Nucl. Phys. A **101**, 1 (1967).
[7] D. J. Millener, Nucl. Phys. A **693**, 394 (2001), and private communication.
[8] T. R. Fisher, S. S. Hanna, D. C. Healey, and P. Paul, Phys. Rev. **176**, 1130 (1968).
[9] C. N. Davids *et al.*, Nucl. Instrum. Methods Phys. Res., Sect. B **70**, 358 (1992).
[10] I-Yang Lee, Nucl. Phys. A **520**, 641c (1990).
[11] J. F. Ziegler, J. P. Biersack, and M. D. Ziegler, *SRIM: The Stopping of Ions in Matter* (Lulu Press, Morrisville, NC, 2008), http://www.srim.org.
[12] H. Paul and A. Schinner, Nucl. Instrum. Methods Phys. Res., Sect. B **195**, 166 (2002).
[13] D. E. Alburger, E. K. Warburton, A. Gallmann, and D. H. Wilkinson, Phys. Rev. **185**, 1242 (1969).
[14] B. A. Brown and B. H. Wildenthal, Annu. Rev. Nucl. Part. Sci. **38**, 29 (1988).
[15] A. Umeya, G. Kaneko, and K. Muto, Nucl. Phys. A **829**, 13 (2009).
[16] S. C. Pieper and R. B. Wiringa, Annu. Rev. Nucl. Part. Sci. **51**, 53 (2001).
[17] S. C. Pieper, K. Varga, and R. B. Wiringa, Phys. Rev. C **66**, 044310 (2002).
[18] M. Pervin, S. C. Pieper, and R. B. Wiringa, Phys. Rev. C **76**, 064319 (2007).
[19] R. B. Wiringa, Phys. Rev. C **73**, 034317 (2006).
[20] R. B. Wiringa, V. G. J. Stoks, and R. Schiavilla, Phys. Rev. C **51**, 38 (1995).
[21] S. C. Pieper, AIP Conf. Proc. **1011**, 143 (2008).
[22] B. S. Pudliner, V. R. Pandharipande, J. Carlson, and R. B. Wiringa, Phys. Rev. Lett. **74**, 4396 (1995).
[23] W. Nörtershäuser *et al.*, Phys. Rev. Lett. **102**, 062503 (2009).
[24] E. Caurier, P. Navrátil, W. E. Ormand, and J. P. Vary, Phys. Rev. C **66**, 024314 (2002).
[25] C. Forssáen, R. Roth, and P. Navrátil, arXiv:1110.0634v2.
[26] P. Navrátil (private communication).
[27] R. Machleidt, Phys. Rev. C **63**, 024001 (2001).
[28] L. Liu, T. Otsuka, N. Shimizu, Y. Utsuno, and R. Roth, arXiv:1105.2983v2.
[29] T. Neff and H. Feldmeier, Nucl. Phys. A **738**, 357 (2004).
[30] T. Neff (private communication).
[31] Y. Kanada-En'yo and H. Horiuchi, Phys. Rev. C **55**, 2860 (1997).
[32] Y. Kanada-En'yo, Phys. Rev. C **71**, 014310 (2005).
[33] G. Hagen, T. Papenbrock, D. J. Dean, and M. Hjorth-Jensen, Phys. Rev. C **82**, 034330 (2010).
[34] E. Epelbaum, H. Krebs, D. Lee, and Ulf-G. Meissner, Phys. Rev. Lett. **104**, 142501 (2010).
[35] E. Epelbaum, H. Krebs, D. Lee, and Ulf-G. Meissner, Phys. Rev. Lett. **106**, 192501 (2011).